Noise model for polarization-sensitive optical coherence tomography*

Paul A. Williams[1], Nate J. Kemp[2], David Ives[3], Jesung Park[2], Jordan C. Dwelle[2], H. Grady Rylander III[2], and Thomas E. Milner[2]

[1]*National Institute of Standards and Technology, 325 Broadway, Boulder, CO 80305, (303) 497-3805, pwilliam@boulder.nist.gov*
[2]*The University of Texas at Austin, Department. of Biomedical Engineering, 1 University Station #C0800, Austin, Texas 78712*
[3]*National Physical Laboratory, Teddington, Middlesex, United Kingdom, TW11 0LW*

ABSTRACT

Characterizing and quantifying noise sources in birefringence imaging with polarization-sensitive optical coherence tomography (PS-OCT) is necessary for the development of efficient noise reduction techniques for real-time clinical PS-OCT imaging. We propose three noise regimes based on the strength of specimen backscattering and dominated by different noise sources. We introduce a model that predicts noise effects in two regimes. The model includes source/detector intensity noise, and couples speckle effects with the longitudinal delays due to instrument and specimen birefringence to create realistic noise on simulated orthogonal interference fringe amplitudes and on their relative phases. Experimental examples of the three regimes are presented and in two of them, qualitative agreement between the model and experimental data is demonstrated.

Keywords: birefringence, noise, optical coherence tomography, polarization, PS-OCT, speckle

1. INTRODUCTION

Polarization-sensitive optical coherence tomography[1] (PS-OCT) has been shown to provide highly sensitive estimates of birefringence, biattenuance[2] and optic axis orientation[3] in fibrous tissue. Sufficient polarimetric signal-to-noise ratio[4] (PSNR) and high sensitivity is achieved by ensemble averaging and nonlinear fitting of normalized Stokes vector arcs on the Poincaré sphere acquired for multiple launched polarization states.[4] High acquisition speed and real-time image generation are desired for clinical application of PS-OCT, which necessitates improved efficiency in noise reduction and data processing. However, sources of noise confounding PS-OCT measurements are not completely understood and require further investigation. In this paper, we discuss several noise processes and identify three regimes in which different noise sources dominate PS-OCT measurement uncertainty. We illustrate these regimes with experimental PS-OCT measurements of birefringent tendon. A preliminary model is presented that qualitatively predicts noise in two of the three regimes–the weakly scattering regime and the strong single-scattering regime–and will guide future development of efficient noise reduction techniques.

2. METHODS AND MODEL

PS-OCT data typically consist of depth-resolved fringe amplitudes [$\Gamma_h(z)$ and $\Gamma_v(z)$] and relative phase [$\phi_{v\text{-}h}(z)$] of detected interference signals in two orthogonal polarization modes (e.g., horizontal and vertical), where z is the penetration depth into the sample. $\Gamma_h(z)$, $\Gamma_v(z)$, and $\phi_{v\text{-}h}(z)$ are determined by coherent demodulation or Hilbert transform techniques in time-domain PS-OCT or Fourier transform in spectral-domain PS-OCT.[5] Analytical methods involving Jones-matrix analysis[6,7] or geometrical methods involving Stokes vectors and the Poincaré sphere[4,8] can then be used to estimate relevant specimen polarization properties [birefringence (Δn), biattenuance ($\Delta\chi$), or optic axis orientation (θ)].

For measurement results given in the form of the output Stokes vector as a function of penetration depth $\boldsymbol{S}(z)$, the noise can be quantified by use of the speckle standard deviation[4]

$$\sigma_{speckle} = \left(\frac{1}{J} \sum_{j} \{ \cos^{-1}[\mathbf{S}(z_j) \cdot \mathbf{P}(z_j)] \}^2 \right)^{1/2}, \quad (1)$$

where $\boldsymbol{P}(z)$ is the expected Stokes vector in the absence of noise and the sum is over the total number of depth-resolved samples J in the birefringent specimen. Here, we propose three noise regimes, based on the strength of specimen backscattering, in which different noise sources dominate $\sigma_{speckle}$ and thus PS-OCT measurement uncertainty. These three regimes are illustrated by experimental PS-OCT measurements of birefringent rat tail tendon in solutions of varying concentrations of glycerol and phosphate-buffered saline (PBS). Using a commercial refractometer, we found that varying the glycerol concentration allowed us to change the refractive index of the solution from 1.33 for pure PBS to 1.47 for pure glycerol. Estimating the refractive index of the protein in the tendon to be 1.53 indicates that increasing the glycerol concentration will reduce the amount of light scattering (due to a reduced index mismatch between tendon and solution) and reduce the birefringence of the tendon. This second effect comes about because the tendon optical anisotropy is dominated by a form birefringence (due to the shape of the fibrous tendons) that has been shown to depend inversely on the refractive index mismatch between the tendon and the surrounding medium.[9] Experimental measurements were made with the PS-OCT system described in Reference 4, with a specimen depth of 170 μm and at a measurement wavelength of 830 nm (55 nm FWHM).

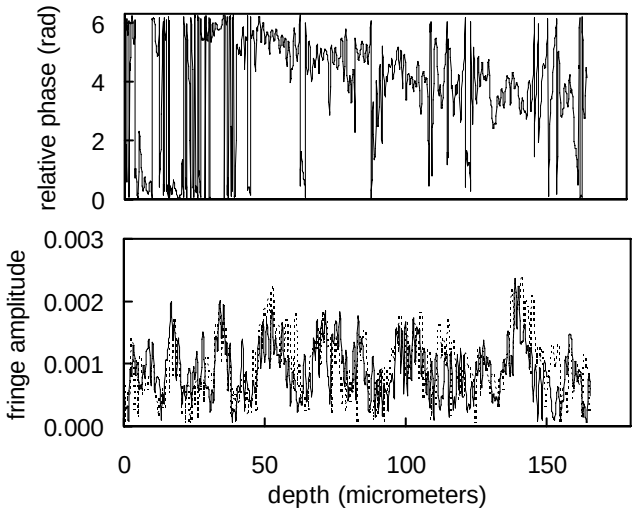

Figure 1a. Regime I (measured), source/detector noise dominates (tendon in 75 % glycerol). Solid (h), dashed (v).

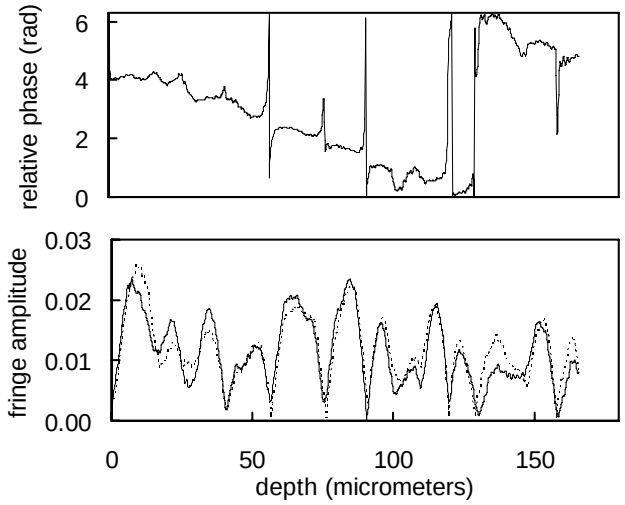

Figure 1b. Regime II (measured), path birefringence dominates, (tendon in 31 % glycerol). Solid (h), dashed (v).

2.1 Scattering regime I – low scattering: Experimental results

Regime I is illustrated in Figure 1a by relative phase and amplitude envelope profiles from a PS-OCT measurement of tendon in a solution of 75 % glycerol and 25 % PBS (by volume). A refractive index of 1.44 was measured for the solution and a specimen birefringence $\Delta n = 0.0016$ was determined from the PS-OCT measurement. The high refractive index significantly reduces specimen backscattering (producing a weak OCT interference signal). Thus noise in the optical source or the detector contributes significantly to the measured phase and fringe envelopes, dominating the uncertainty in the determination of the state of polarization (SOP).

2.2 Scattering Regime II – single-scattering: Experimental results

Regime II is illustrated in Figure 1b from a PS-OCT measurement of tendon in a solution of 31 % glycerol and 69 % PBS. The solution's refractive index was 1.38; the tendon birefringence was $\Delta n = 0.003$. Here, specimen backscattering is increased sufficiently to bring the detected OCT signal amplitude well above the source/detector noise floor. Now, the fringe amplitudes (speckle patterns) are very similar for the two orthogonal polarization modes. Because the axis of specimen birefringence is co-aligned with the horizontal plane, the overall slope of the phase with scan depth is a measure of the material birefringence. The characteristic spikes on the phase come at points where the fringe amplitude of one polarization state is near

zero, dramatically increasing the uncertainty in calculated phase. We postulate that the majority of the returning photons measured in this regime have experienced a single back-scattering event.

2.3 Scattering Regime III – multiple scattering: Experimental results

Regime III is illustrated in figure 1c from a PS-OCT measurement of tendon in a pure PBS solution (refractive index 1.33). The tendon birefringence was measured to be $\Delta n = 0.0044$. Now the phase profile is no longer the simple sloped line and narrow spikes of regime II, but has slowly varying distortions that make the determination of the slope more difficult. We speculate that in this highly scattering regime, light in the return path has experienced multiple back-scattering events before leaving the specimen.

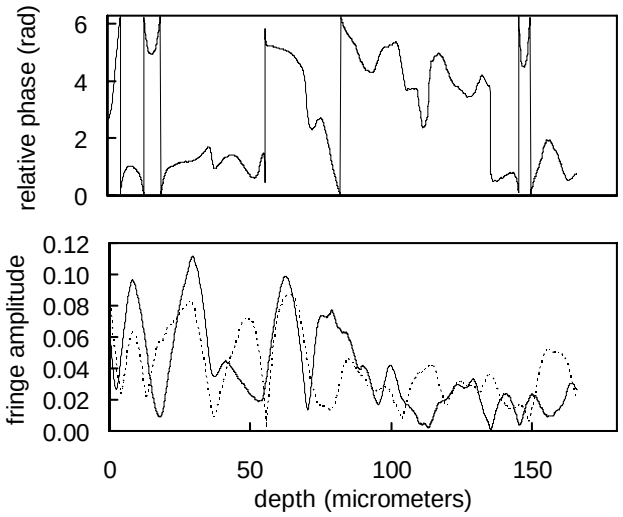

Figure 1c. Regime III (measured), polarization-dependent scattering dominates, (native tendon). Solid (h), dashed (v).

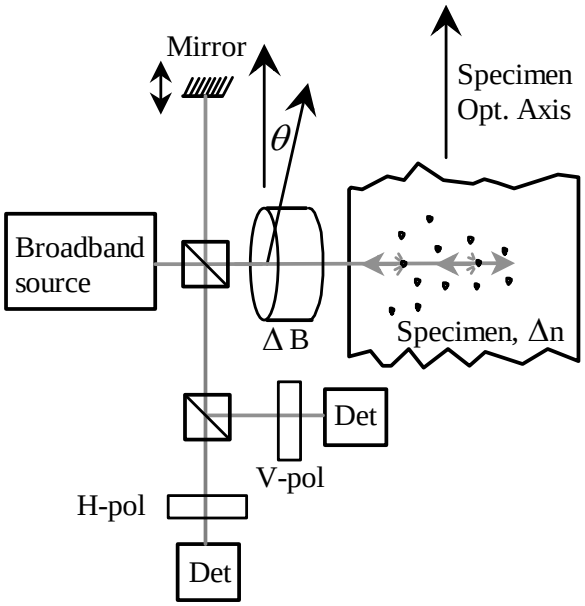

Figure 2. Schematic representation of PS-OCT system in our computer simulation. ΔB is the strength of the internal birefringence (shown schematically as a waveplate), H-pol and V-pol are the linear polarizers, Det = detector.

2.4 Simulation description

Our simulation models the PS-OCT instrument used to generate the data of figures 1a, 1b, and 1c. The simulation geometry is shown schematically in Figure 2. We modeled a broadband light source (center wavelength 830 nm, FWHM 55 nm), an isotropic (birefringence-free) reference arm with moveable mirror, and a specimen arm with an inherent birefringence ("instrument birefringence") described by its polarization-dependent path length difference ΔB (units of distance) oriented at an angle θ with respect to the optic axis of the specimen. In practice, instrument birefringence can arise from a launch polarization controller, stray birefringence in the system, or any specimen birefringence preceding the region being measured such as that experienced when using single-mode fiber-optic light delivery to the specimen. We simulated a non-polarizing beamsplitter launching the input light into the specimen and reference arms and recombining the returning light, which is split onto two orthogonal polarizers followed by detectors. The detector polarizations were assumed to be oriented so that one is aligned with the optic axis of the specimen.

The specimen was modeled as a homogenous, linearly birefringent element with birefringence Δn and N scattering points randomly spaced along the length of the specimen. The longitudinal positions of the scattering points were randomly chosen from a uniform spatial distribution. We used Jones matrices to propagate the electric field into the specimen and reflect a portion of the light amplitude at each scattering point. We assumed that the light in each return path has experienced only one backward scattering event. We modeled each scattering event as a mirror whose reflectance has negligible effect on the amount of light propagating in the forward direction and is independent of polarization. The modeled scattering points do not modify the polarization state upon reflection. The specimen birefringence has orthogonal axes ***h*** and ***v***. The complete back-propagating electric field due to scattering was calculated in the frequency domain as a summation over the N scattering points and represented in Jones vector notation as

$$\mathbf{E}_{\mathrm{sig}}(\omega) = \tfrac{1}{2} r E_0(\omega) e^{i\frac{\omega}{c}2zf} \mathbf{R}_{\mathrm{b}} \sum_{j=1}^{N} \begin{bmatrix} e^{i\frac{\omega}{c}(2n+\Delta n)z_j} & 0 \\ 0 & -e^{i\frac{\omega}{c}(2n-\Delta n)z_j} \end{bmatrix} \mathbf{R}_{\mathrm{f}} \begin{pmatrix} \frac{1}{\sqrt{2}} \\ \frac{1}{\sqrt{2}} \end{pmatrix}, \quad (2)$$

where ω is the radian frequency of the light, r is the reflectance from a single scatterer, E_0 is the electric field source spectrum (Gaussian shape), c is the speed of light in vacuum, zf is the distance from the beamsplitter to the front surface of the specimen, n is the mean refractive index of the specimen, Δn is the specimen birefringence, and z_j is the position of the j^{th} scattering point within the specimen. The matrices $\mathbf{R_f}$ and $\mathbf{R_b}$ represent the forward and backward Jones matrices of the internal birefringence, given by

$$\mathbf{R}_f = \begin{bmatrix} \cos^2(\theta)\, e^{i\frac{\omega}{c}\frac{\Delta B}{2}} + \sin^2(\theta)\, e^{-i\frac{\omega}{c}\frac{\Delta B}{2}} & i\sin(2\theta)\sin(\frac{\omega}{c}\frac{\Delta B}{2}) \\ i\sin(2\theta)\sin(\frac{\omega}{c}\frac{\Delta B}{2}) & \cos^2(\theta)\, e^{-i\frac{\omega}{c}\frac{\Delta B}{2}} + \sin^2(\theta)\, e^{i\frac{\omega}{c}\frac{\Delta B}{2}} \end{bmatrix}, \quad (3)$$

where ΔB is as defined above (for example, a quarter-wave of birefringence at wavelength λ_0 would be given as $\Delta B = 0.25\lambda_0$). θ is the angle between the optic axis of the instrument birefringence and the optic axis of the specimen birefringence. $\boldsymbol{R}_{\mathbf{b}}$ is similar to $\boldsymbol{R}_{\mathbf{f}}$ but with a sign change on the top right and bottom left elements.

Using a standard representation for the electric field in the reference arm, we calculated the intensity at each detector, performed a Fourier transform, and found the orthogonal fringe amplitudes [$\Gamma_h(z)$ and $\Gamma_v(z)$] and relative phase [$\phi_{v\text{-}h}(z)$].

To simulate the effects of optical source or detector noise, we explicitly added a Gaussian-distributed noise to the interferometric intensity signals. We quantified the noise level in terms of the signal-to-noise ratio (SNR) of the square of the fringe envelope.

3. RESULTS

By varying the parameters of our simulation, we were able to generate relative phase and fringe envelopes as a function of sampling depth. By modifying the amount of source/detector noise (quantified by signal-to-noise ratio SNR) and the specimen birefringence, we obtained results comparable to scattering regimes I and II.

3.1 Scattering Regime I: Simulation results

To mimic the noise behavior of Regime I, we set SNR = 23 dB, specimen birefringence Δn = 0.0016, N=100 scattering points, a specimen length of 170 μm, and no instrument birefringence (ΔB=0, θ=0). We obtained the results shown in Figure 3a. The simulated relative phase and fringe envelopes show noise behavior qualitatively similar to the experimental results of Figure 1a. In order to quantify the noise, we calculated the PSNR for both the experimental and simulated results of Regime I. The experimental data of figure 1a yielded a polarization signal-to-noise ratio[4] (PSNR) of 30 (on a data set consisting of 64 averaged A-scans). Assuming that in Regime I, PSNR scales as $N_S^{1/2}$ (where N_S is the number of A-scans), we can adjust this number to give a single A-scan PSNR of 3.75. Our simulation yielded a single A-scan PSNR of 7. Comparing these values, the simulation predicts the noise to be lower by about a factor of 2. This could be due to other sources of experimental noise not yet included in the model.

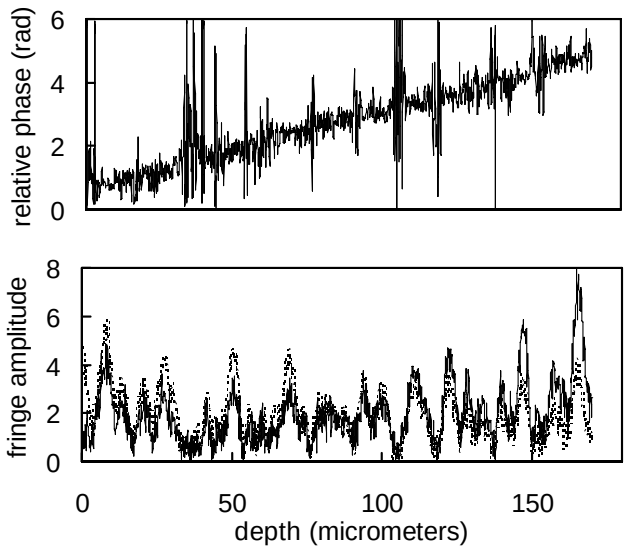

Figure 3a. Regime I (simulated), SNR = 23 dB, Δn=0.0016, ΔB=0. Solid (h), dashed (v).

3.2 Scattering Regime II: Simulation results

In Regime II, the scattering is strong enough that the source/detector noise no longer dominates the phase uncertainty. In this regime, polarization speckle is the dominant noise source. In the absence of speckle-noise effects, the measured output SOP trajectory should be an arc on the Poincaré sphere corresponding to a smooth slope of the phase-versus-depth curve. However, the presence of birefringence in the specimen differentially delays the interference fringe patterns of the two orthogonal polarization modes. In the presence of speckle, these delays introduce a shift between the speckle patterns $\Gamma_h(z)$ and $\Gamma_v(z)$ and generate small differences between their local amplitudes. The effect of this shift is small when both $\Gamma_h(z)$ and $\Gamma_v(z)$ are sufficiently large. But when one envelope is near zero, the uncertainty of the calculated phase drastically increases, causing a spike in the phase-versus-depth profile (and a loop on the Poincaré sphere). These spikes are seen in the experimental data of Figure 1b. We achieve good qualitative agreement with this result through simulation (SNR = 55 dB, Δn = 0.003, N=100, L=170 μm, ΔB=0, and θ=0), see Figure 3b. The experimental PSNR for Regime II is 70 (for 64 averaged A-scans). As in Regime I, we scale this to the equivalent single A-scan PSNR of 8.75. Our simulation yields a single A-scan PSNR of 27. Again, the experiment yields more noise than predicted by theory. This time, the difference is a factor of 3. Since we have not developed a quantitative metric to distinguish the noise regimes, it is possible that our experimental results for Regime II are actually experiencing some noise from Regime III (which is not yet included in our simulation). As discussed in the next section, we do not yet have a mechanism to describe the Regime III noise. When we develop the third noise mechanism and include it in our model, we expect to improve the agreement between simulation and experiment for all the regimes.

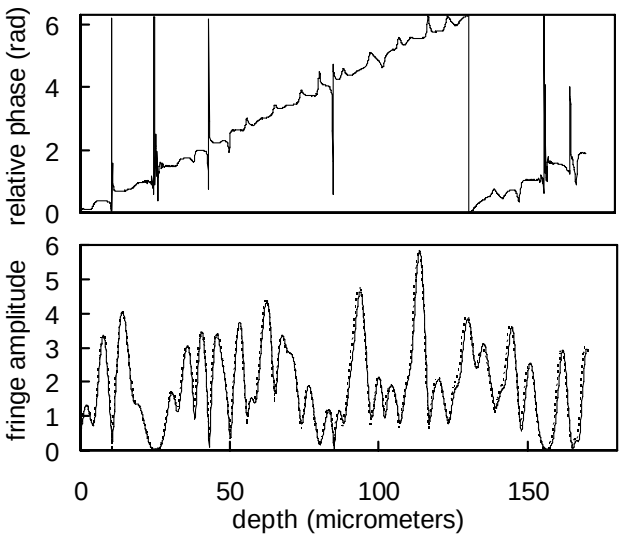

Figure 3b. Regime II (simulated), SNR = 55 dB, Δn=0.003, ΔB=0. Solid (h), dashed (v).

3.3 Scattering Regime III: discussion

So far, we have been unable to obtain simulation results that resemble the experimental data of Regime III (Figure 1c). The key feature seems to be that the fringe amplitudes $\Gamma_h(z)$ and $\Gamma_v(z)$ are significantly decorrelated. Neither the source/detector noise of Regime I, the polarization speckle of Regime II, nor the misaligned instrument birefringence of Figure 4 are able to produce this result. As mentioned, the scattering in Regime II is assumed to be single-back-scattering. This results in a polarization-independent scattering. It is our hypothesis that Regime III has a sufficiently high backscattering cross section that it will have a significant number of multiple-back-scattered events in the returned light. This introduces a polarization-dependent scattering which, when coupled with the speckle, could produce the results seen. Additional work is planned to pursue this hypothesis.

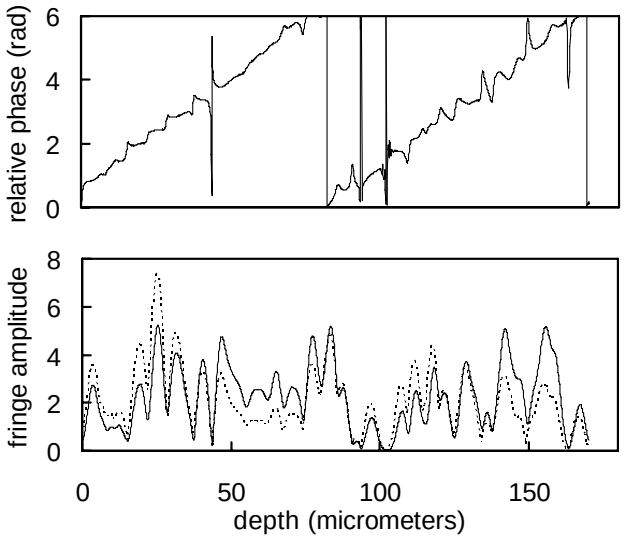

Figure 4. Simulated relative phase and fringe amplitude profiles due to instrument birefringence, $\Delta B=0.1\lambda_0$, Δn=0.0045, θ=30°. Solid line (v), dashed line (h).

3.4 Effects of instrument birefringence

The birefringence-induced shifts between the fringe amplitudes $\Gamma_h(z)$ and $\Gamma_v(z)$ can become large when instrument birefringence (ΔB) is nonzero. Fortunately, when θ=0, this longitudinal shift and the resulting phase spikes can be substantially removed by adding a constant shift to $\Gamma_h(z)$ or $\Gamma_v(z)$ in software (if other sources of noise are sufficiently small to

allow the appropriate shift to be determined). However, if θ is nonzero, then the effects of instrument birefringence cannot be easily removed. The most likely measurement scenario is that there is some instrument birefringence with a misalignment between it and the specimen ($\theta \neq 0$). This could occur if the optic axis of the polarization controller birefringence is not exactly aligned with the optic axis of the specimen birefringence, or if the probe light has to travel through birefringent layers in the specimen (of different alignment) before reaching the area of measurement. This is the case for retinal measurements, where the cornea of the eye exhibits birefringence. We model the unaligned case with $\Delta B=0.1\lambda_0$, $\Delta n=0.0045$, $N=100$, $L=170$ μm, and $\theta=30°$. Figure 4 shows the effects of both longitudinal shifts and large fringe amplitude differences (due to both speckle variation between ***h*** and ***v*** and due to misalignment of the returning state with the detector axes). These complicated differences in the speckle patterns cannot be easily removed in software and result in significant distortions to the phase. Therefore, care should be taken experimentally to reduce the instrument birefringence as much as possible (possibly by use of an optical compensator).

3.5 Noise behaviour

In order to check the validity of our noise model we measured the effect of averaging multiple measurements to reduce polarization speckle noise. In Reference 2 it is shown that normalized PSNR ("PSNR gain") increases as the $N_S^{1/2}$, where N_S is the number of A-scans averaged. We simulated averages of multiple statistically independent measurements of a specimen 80 μm long, with birefringence $\Delta n=0.005$ and negligible source/detector noise. Figure 5 demonstrates that the simulation produces the predicted $N_S^{1/2}$ dependence.

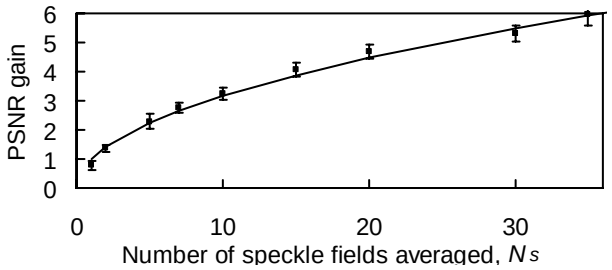

Figure 5. Simulated ensemble averaging of N_s uncorrelated speckle fields (A-scans). Points are the simulation results, error bars give the standard deviation of 10 repeated simulations, solid line is $N_s^{1/2}$.

In Regime I, the relationship between SNR (due to the source/detector noise) and the resulting phase noise is expected to behave as

$$\sigma_{phase} = SNR^{-1/2}, \tag{4}$$

(where σ_{phase} is the standard deviation of the phase $\phi_{v\text{-}h}$ at a fixed position)[5]. We tested this experimentally with repeated PS-OCT measurements of the phase $\phi_{v\text{-}h}$ from a mirror surface as the SNR was varied by inserting different neutral-density filters in the specimen arm. We also simulated this measurement. Figure 6 illustrates the agreement. The agreement is good, except for some deviation of the experimental results for the largest values of SNR. The deviation from theory at low SNR for both the simulation and experimental results is to be expected since the derivation[5] of Equation (4) assumes a sufficient SNR (nominally above 20 dB). However, at present, we have no explanation for the experimental deviation seen at large SNR.

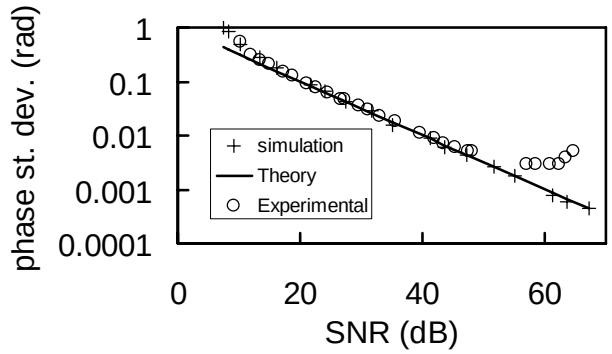

Figure 6. Experimental, theoretical (Ref. 5), and simulated dependence of phase noise on SNR.

4. CONCLUSION

The simulated results for Regimes I and II agree qualitatively with experiment. Our preliminary noise model uses polarization-independent scattering to estimate measurement uncertainty due to source/detector noise, instrument birefringence and misalignment. Future work will involve more rigorous quantification of the various scattering regimes and the addition of polarization-dependent scattering processes.

REFERENCES

1. Johannes F. de Boer, Thomas E. Milner, Martin J.C. van Gemert, J. Stuart Nelson, “Two-dimensional birefringence imaging in biological tissue by polarization-sensitive optical coherence tomography,” *Optics Letters*, **22**(12), 934-936 (1997).
2. N. J. Kemp, H. N. Zaatari, J. Park, H. G. Rylander, and T. E. Milner, "Form-biattenuance in fibrous tissues measured with polarization-sensitive optical coherence tomography (PS-OCT)," *Optics Express*, **13**(12), 4611-4628 (2005).
3. Nate J. Kemp, Haitham N. Zaatari, Jesung Park, H. Grady Rylander III, and Thomas E. Milner, "Depth-resolved optic axis orientation in multiple layered anisotropic tissues measured with enhanced polarization-sensitive optical coherence tomography (EPS-OCT)," *Optics Express*, **13**(12), 4507-4518 (2005).
4. N. J. Kemp, J. Park, H. N. Zaatari, H. G. Rylander, and T. E. Milner, "High sensitivity determination of birefringence in turbid media using enhanced polarization-sensitive Optical coherence tomography," *Journal of the Optical Society of America A*, **22**(3), 552-560 (2005).
5. B. H. Park, M. C. Pierce, B. Cense, S. H. Yun, M. Mujat, G. J. Tearney, B. E. Bouma, and J. F. de Boer, "Real-time fiber-based multi-functional spectral-domain optical coherence tomography at 1.3um," *Optics Express*, **13**(11), 3931-3944 (2005).
6. B. H. Park, M. C. Pierce, B. Cense, and J. F. de Boer, "Jones matrix analysis for a polarization-sensitive optical coherence tomography system using fiber-optic components," *Optics Letters*, **29**(21), 2512-2514 (2004).
7. S. Jiao and L. V. Wang, "Jones-matrix imaging of biological tissues with quadruple-channel optical coherence tomography," *Journal of Biomedical Optics*, **7**(3), 350-358 (2002).
8. C. E. Saxer, J. F. de Boer, B. H. Park, Y. Zhao, Z. Chen, and J. S. Nelson, "High-speed fiber-based polarization-sensitive optical coherence tomography of in vivo human skin," *Optics Letters*, **25**(18), 1355-1357 (2000).
9. Rudolf Oldenbourg and Teresa Ruiz, “Birefringence of macromolecules,” *Biophysics Journal*, 56, 195-205 (1989).